



Cite this: DOI: 10.1039/d0cp04347h

Crystal facet-dependent activity of h-WO₃ for selective conversion of furfuryl alcohol to ethyl levulinate†

 Guoming Gao,^a Mingxuan Lv,^a Yuewen Shao,^a  Guanggang Gao,^a  Hui Zhao,^b Shu Zhang,^c Yi Wang,^d  Ran Duan,^e Qifeng Chen *^a and Xun Hu *^a

The use of WO₃ as an acid catalyst has received extensive attention in recent years. However, the correlation between the catalytic activity and the predominantly exposed surface with varied acidic sites needs further understanding. Herein, the effects of the Brønsted and Lewis acid sites of different crystal facets of WO₃ on the catalytic conversion of furfuryl alcohol (FA) to ethyl levulinate (EL) in ethanol were investigated in detail. A yield of EL up to 93.3% over WO₃ with the (110) facet exposed was achieved at 170 °C, while FA was mainly converted to polymers over (001) faceted nanosheets and nanobelts with exposed (002) and (100) facets. This was attributed to the different distribution of the acidic sites on different exposed crystal facets. The (110) faceted WO₃ possessed abundant and strong Brønsted acid sites, which favored the conversion of FA to EL, while the (100) faceted WO₃ with stronger Lewis acid sites and weaker Brønsted acid sites mainly led to the formation of polymers. In addition, the (110) faceted WO₃ showed excellent sustainability in comparison with the (100) faceted counterpart.

 Received 17th August 2020,
 Accepted 2nd November 2020

DOI: 10.1039/d0cp04347h

rsc.li/pccp

Introduction

Tungsten trioxide (WO₃) is a versatile material with wide applications in gas sensing,¹ (photo)catalysis,^{2,3} electrocatalysis and so on,^{4–6} due to its moderate band gap semiconductivity, stability in solvents and other excellent physical and chemical properties.^{7,8} WO₃ has been used as an acid catalyst for esterification of oleic acid,⁹ preparation of biodiesel,¹⁰ conversion of glycerol,¹¹ preparation of fructose¹² and fatty acid esterification.¹³ WO₃-based catalysts show promising catalytic activity due to the presence of Brønsted and Lewis acid sites.¹⁴

The distributions of Brønsted and Lewis acid sites are closely related to the configuration of the atoms on the surface of WO₃. Therefore, the exposed WO₃ crystal facets are highly essential to the formation of acid sites, which can further influence the catalytic performance of WO₃ catalysts. The effects

of the exposed crystal facets on the catalytic performances of WO₃ catalysts have been reported in catalytic reactions.^{15–17} Xie *et al.* reported that WO₃ with a proper proportion of (002), (200) and (020) showed much higher photocatalytic oxidation activity of H₂O for oxygen evolution than other exposed facets.¹⁶ Wang *et al.* stated that hexagonal WO₃ (h-WO₃) nanosheets with an exposed (001) facet exhibited superior visible photocatalytic activity due to the promoted charge separation efficiency on the high energy (002) facet.¹⁷ It is well known that the chemical composition and states of the exposed crystal surface could significantly influence the reactivity of WO₃ catalysts.¹⁸ Therefore, the correlation between the reactivity and chemical composition and states of the WO₃ surface should be deeply explored and understood. However, there are to date few studies focusing on understanding the correlation between the reactivity and the specific crystal facets of WO₃ combined with the distribution of acid sites. The demonstration of such a correlation, therefore, is of great significance for designing highly efficient WO₃-based solid acid catalysts.

Herein, we synthesized WO₃ with the (001), (100) and (110) crystal facets exposed *via* a hydrothermal method and explored the facet effects on the catalytic performances in the catalytic conversion of furfuryl alcohol (FA), an organic compound produced from the hydrogenation of biomass-derived furfural, to ethyl levulinate (EL), a platform chemical for manufacturing other value-added chemicals. It was found that (110) faceted WO₃ showed the highest catalytic activity with a 93.3% yield of EL,

^a School of Material Science and Engineering, University of Jinan, Jinan, 250022, China. E-mail: qfchen@126.com, Xun.Hu@outlook.com

^b Institute of Surface Analysis and Chemical Biology, University of Jinan, Jinan, 250022, P. R. China

^c College of Materials Science and Engineering, Nanjing Forestry University, Nanjing 210037, Jiangsu, China

^d State Key Laboratory of Coal Combustion, Huazhong University of Science and Technology, Wuhan, 430074, China

^e Institute of Chemistry Chinese Academy of Sciences, Beijing, 100190, China

† Electronic supplementary information (ESI) available. See DOI: 10.1039/d0cp04347h

while (100) faceted WO_3 nanobelts mainly catalyzed the polymerization of FA. WO_3 nanosheets with the (001) facet exposed showed the worst activity, due to the presence of the smallest number of acidic sites on the (001) facet. The acid sites on the different exposed crystal facets were characterized by temperature programmed desorption with ammonia, and pyridine adsorption diffuse reflectance infrared Fourier transform spectroscopy (DRIFTS), and the distributions of acid sites were well correlated with the catalytic performances.

Experimental

Materials

All reagents used in this work were analytical grade. FA, EL, ethanol, $\text{Na}_2\text{WO}_4 \cdot 2\text{H}_2\text{O}$ and ammonium paratungstate (APT) were bought from Shanghai Macklin Biochemical Co., Ltd. Urea, thiourea and citric acid were bought from Sinopharm Chemical Reagent Co., Ltd.

Catalyst preparation

Hydrothermal synthesis of h- WO_3 nanosheets (001). h- WO_3 nanosheets with the (001) facet exposed were prepared *via* a hydrothermal method.¹⁹ Specifically, 1.000 g of $\text{NaWO}_4 \cdot 2\text{H}_2\text{O}$ and 0.300 g of urea were dissolved respectively in 30 mL of deionized water (H_2O). The two solutions were blended in a beaker after stirring for 30 min and stirred for 30 min. After that, 6.0 mol L^{-1} HCl aqueous solution was slowly added into the mixed solution by using a buret, and the pH of the solution was monitored with a pH meter. When the pH decreased to 1.5, the speed of addition of the acid solution was slowed down and stopped at a pH of 1.0. The solution then was moved into a Teflon-lined autoclave, sealed and placed in an oven at 180 °C for 12 h. Then, the samples were washed with deionized ethanol and water three times, respectively. The obtained samples were transferred into a vacuum oven to dry at 60 °C for 10 h for use in the catalytic conversion of FA.

Hydrothermal synthesis of h- WO_3 nanobelts (100). h- WO_3 nanobelts were prepared by a hydrothermal method.²⁰ Firstly, 2.000 g of APT and 800 mg of citric acid were dissolved respectively in 30 mL of deionized water. The two solutions were mixed in a beaker and stirred for 2.0 h after stirring for 60 min. Finally, the solution was loaded in a Teflon-lined autoclave and hydrothermally treated in a drying oven (180 °C, 12 h). After the reaction finished, the samples were washed with deionized ethanol and water three times, respectively. The obtained samples were transferred into a vacuum oven to dry at 60 °C for 10 h for use in the catalytic conversion of FA.

Synthesis of h- WO_3 nanoparticles (110)

h- WO_3 nanoparticles were prepared by a precipitation and hydrothermal method.²¹ Firstly, 5.000 g of $\text{NaWO}_4 \cdot 2\text{H}_2\text{O}$ was dissolved in 30 mL of deionized water. After stirring for 60 min, the pH of the solution was adjusted to 2.0 using 4.0 mol L^{-1} HCl. After that, the precipitate was then filtered and collected. The precursor was then dried for 12 h in a vacuum drying oven

for use in the catalytic reactions. 0.500 g of tungstic acid and 0.500 g of thiourea were added to 40 mL of deionized water, respectively. After stirring for 60 min, the two solutions were mixed, loaded in a Teflon-lined autoclave and hydrothermally treated in an oven at 180 °C for 24 h. Subsequently, the sediments were collected and washed by centrifugation and the obtained samples were moved into a vacuum oven to remove excess moisture at 60 °C for 10 h for further use.

Catalytic experiments

Evaluation of the catalytic activities of the catalysts in the acid-catalyzed conversion of FA to EL was carried out in an autoclave reactor made of 316 stainless steel. In a typical experiment, 0.040 g of catalyst and 0.4 mmol of FA were mixed with 3.960 g of ethanol in the reactor vessel (10 mL). The autoclave reactor then was closed, and the residual air inside was removed *via* flushing with nitrogen three times. After that, the reactor was pressurized with nitrogen to 4.0 MPa and was then heated to the preset temperature in *ca.* 30 min. The reaction time was typically set at 2 h at the preset reaction temperature. The reaction system was magnetically stirred with a speed of 400 rpm during the reaction. After finishing the experiment, the reactor was cooled with circulating water to room temperature. Afterwards, the collected solid was washed with ethanol and water, and then dried overnight at 60 °C for further analysis.

Catalyst characterization

High-resolution transmission electron microscopy (HRTEM) images and transmission electron microscopy (TEM) images were observed on a JEOL2100Plus, which was used to analyze the morphologies and microstructures of the WO_3 catalysts.

To analyze the phase composition of the WO_3 catalysts with different crystal facets exposed, X-ray diffraction (XRD) was conducted on an X-ray powder diffractometer (Rigaku Ultima IV type, Cu $\text{K}\alpha$ target, $\lambda = 0.154$ nm). The 2θ scanning range applied was from 5 to 80° with a scanning speed of 10° min^{-1} .

To analyze the microstructure of the samples, N_2 adsorption-desorption characterizations were performed on a BIAODE SSA-6000 at 77 K. The samples were treated firstly in a vacuum at 200 °C for 2 h to remove the physically adsorbed water and organic compounds. Then the samples adsorbed N_2 to achieve the adsorption-desorption equilibrium. The specific surface area and pore size distribution of the material were calculated by the method of Brunauer-Emmett-Teller (BET) and Barrett-Joyner-Halenda (BJH), respectively.

Photoluminescence (PL) spectra were measured on an RF-6000 fluorescence spectrometer (Shimadzu), which was used to characterize the defects on the surface of the WO_3 catalysts. An ESP 300E spectrometer was used to collect the electron paramagnetic resonance (EPR) signals at 25 °C.

Fourier transform infrared spectroscopy (FTIR) spectra of the samples were measured on a Nicolet iS50 spectrometer. The catalyst and KBr with a weight ratio of 1:200 were mixed together and ground in an agate mortar, and then the sample was pretreated at 105 °C for 4 h to remove the physically

adsorbed components. Finally, the mixed sample was moved to a model and then the model was pressurized to 10 MPa for shaping in the shape of tablet. The tablet sample was characterized in the FTIR spectrometer to analyze the chemical bonds and components.

In addition, X-ray photoelectron spectroscopy (XPS) was carried out to further analyze the chemical compositions and states of the samples, which was performed on a ThermoFischer ESCALAB 250Xi (Al K α , $h\nu = 1486.6$ eV).

To determine the distribution of the acidic sites on the surface of the catalysts, NH₃ temperature programmed desorption (NH₃-TPD) of the catalyst was carried out on a BIAODE PCA-1200 chemisorption instrument. Typically, about 0.050 g of the sample was pretreated at 150 °C for 30 min in a helium flow. When the sample was cooled to 50 °C, NH₃ with a flow of 20 mL min⁻¹ was imported for adsorption. After the adsorption, the physically adsorbed NH₃ was removed by a helium flow with a rate of 20 mL min⁻¹. Finally, the sample was heated to 850 °C in a helium flow (20 mL min⁻¹) at a heating rate of 20 °C min⁻¹. The signal for the desorbed NH₃ was recorded with a TCD detector.

Pyridine absorption *in situ* diffuse reflectance infrared Fourier transform spectroscopy (DRIFTS) of the catalysts contained in a modified Harrick Praying Mantis DRIFT cell was performed to analysis the distribution of Brønsted and Lewis acid sites. Specifically, the sample was filled into the cell, and then the cell was pretreated at 200 °C (30 min, vacuum). The background spectrum was recorded after the sample was cooled to 35 °C. Pyridine then was introduced into the cell with argon gas as a carrier and the adsorption/desorption equilibrium of pyridine on the catalyst surface was achieved at 35 °C for 40 min. The subsequent degassing was performed for 40 min to remove the physically absorbed pyridine. Finally, the cell was heated from 35 °C to 500 °C (10 °C min⁻¹) and the spectra were simultaneously recorded. The ratio of Lewis and Brønsted acid sites was calculated by the method described in a previous report.³²

An ultraviolet (UV) fluorescence spectrometer (Shimadzu, RF-6000) was used to analyze the relative abundance of π -conjugated polymers in the solution after the reactions. The obtained products were diluted with methanol to 400 ppm for further analysis (initial excitation wavelength: 220 nm, initial emission wavelength: 250 nm, scanning speed: 600 nm min⁻¹).

Analysis of the liquid products

The liquid products were analyzed by using a GC-MS (Shimadzu, GCMS-QP2020) equipped with a capillary column (DB-Wax). The identification of the isolated products was carried out *via* mass spectrometry matching using the standard library of NIST 2014. The details of the analysis of the liquid products can be referred to in our previous paper.²² The definitions of the FA conversion and the product yield/selectivity are shown below.

$$\text{FA conversion (\%)} = \frac{\text{Mole of FA consumed}}{\text{Mole of FA loaded}} \times 100\%$$

$$\text{Product yield (\%)} = \frac{\text{Mole of product produced}}{\text{Mole of FA loaded}} \times 100\%$$

$$\text{Product selectivity (\%)} = \frac{\text{Mole of product produced}}{\text{Mole of FA consumed}} \times 100\%$$

Density functional theory (DFT) calculations

The DFT calculations were carried out using the Dmol3 module of the Materials Studio software package. The generalized gradient approximation (GGA) exchange–correlation functional proposed by Perdew, Burke, and Ernzerhof (PBE) was applied during all the calculations, together with the double-numerical basis set plus polarization functions (DNP) with a cutoff value of 3.5 Å. A medium level integration grid and density of states (DOS) *k*-points were employed.

Results and discussion

Microstructure and composition

Fig. 1a1 shows a typical low-magnification TEM image of the synthesized h-WO₃ nanosheets of a thickness of 4–8 nm, in which a couple of nanosheets are overlapped. However, most of the WO₃ nanosheets still maintained the ultra-thin nanosheet structure, as shown in an enlarged TEM image (Fig. 1a2). The clear lattice spacing of 0.390 nm can be attributed to the (001) planes of h-WO₃ [PDF# 75-2187].¹⁹ The evident and regular lattice fringes indicate the high crystallinity of the WO₃ nanosheets, which also can be confirmed by the high and sharp diffraction peaks in the XRD pattern (Fig. 1d). Fig. 1b1 shows typical TEM images of the synthesized WO₃ nanobelts of about 100–800 nm in length and 10–22 nm in thickness. The HRTEM images in Fig. 1b2 reveal the relatively uniform nanoribbon morphology of the sample and the distances of adjacent lattice fringes of 0.383 and 0.634 nm correspond to the (002) and (100) planes of h-WO₃ [PDF# 85-2459].²⁰ In addition, the TEM images in Fig. 1c1 display the spherical nanoparticles with different diameters. Moreover, the HRTEM image in Fig. 1c2 displays a lattice spacing of 0.367 nm for the (110) lattice planes of h-WO₃ [PDF# 33-1387].²¹ In general, the WO₃ nanobelts exposed predominantly the (100) and (002) facets, while the WO₃ nanosheets and WO₃ nanoparticles mainly exposed the (001) and (110) facets, respectively.

The XRD patterns of the WO₃ catalysts are presented in Fig. 1d. For the WO₃ nanosheets, the XRD peaks at 13.9°, 22.7°, 24.4°, 26.9°, 28.2°, 33.6°, 37.7° and 46.7° are the characteristic diffractions of h-WO₃ [PDF# 75-2187].¹⁹ For the WO₃ nanobelts, the peaks at 13.8°, 23.1°, 24.4°, 27.1°, 28.0°, 21.7°, 33.6°, 36.7°, and 47.4° can be assigned to another kind of h-WO₃ [PDF# 85-2459].²⁰ In addition, for the WO₃ nanoparticles, the peaks at 13.8°, 23.1°, 24.4°, 27.3°, 28.2°, 33.6°, 36.7° and 49.9° can be indexed to another kind of h-WO₃ [PDF# 33-1387].²¹ The above XRD data indicate that the three WO₃ catalysts possess the typical h-WO₃ crystal structure. In addition, the high peak intensity of the catalysts indicates the high crystallinity of the

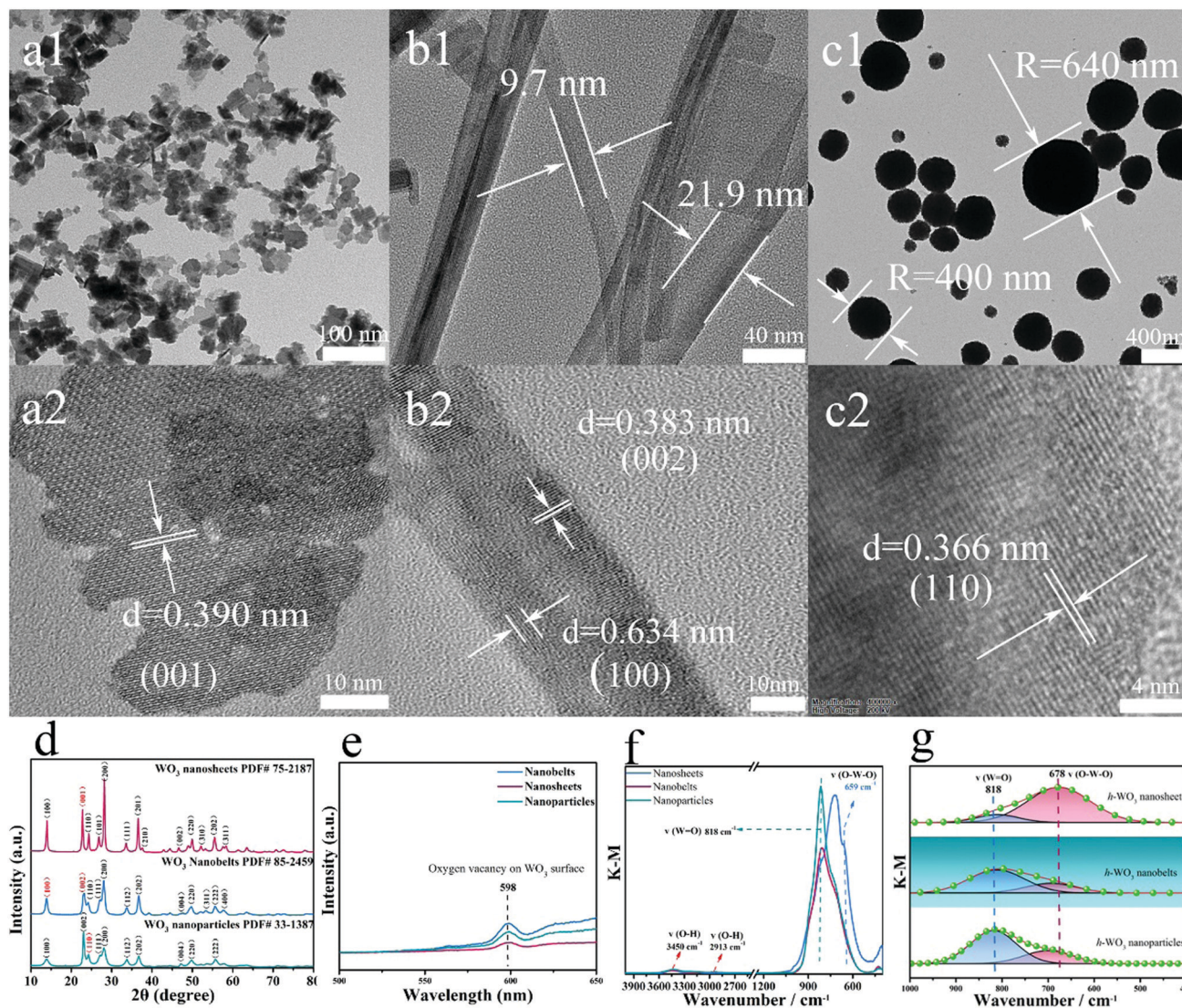


Fig. 1 (a1 and a2) TEM and HRTEM of h-WO₃ nanosheets, (b1 and b2) TEM and HRTEM of h-WO₃ nanobelts, (c1 and c2) TEM and HRTEM of h-WO₃ nanoparticles, (d) XRD patterns of the h-WO₃ catalysts with different morphologies, (e) PL spectra of the h-WO₃ catalysts with different morphologies, and (f and g) FTIR spectra of the h-WO₃ catalysts with different morphologies.

catalysts. The TEM observations combined with the XRD results demonstrate the exposed facets and high crystallinity of the h-WO₃ catalysts.

BET measurements of the samples were conducted to examine the porous nature of the WO₃ catalysts. Fig. S2(a and b) (ESI[†]) show the N₂ adsorption/desorption isotherm and the pore-size distribution (inset) of the WO₃ catalysts. The isotherms of all catalysts are type III, which is characteristic of mesoporous materials.²² According to the Langmuir adsorption principle, the pores in this kind of material are not well developed and the interaction between the catalysts and adsorbed nitrogen molecules is relatively weak.²³ According to the wide pore size distributions of the three WO₃ catalysts, it can be inferred that the specific surface areas of the catalysts are mainly due to the stacking volume among the particles. The results listed in Table 1 show that the WO₃

Table 1 Specific area, pore volume and mean pore radius for the WO₃ catalysts with different morphologies

Entry	Catalysts	Pore volume (cm ³ g ⁻¹)	Mean pore radius (Å)	BET surface area (m ² g ⁻¹)
1	WO ₃ nanoparticles ^a	0.55	201.7	54.7
2	WO ₃ nanobelts ^a	0.29	141.8	40.9
3	WO ₃ nanosheets ^a	0.09	148.5	11.5
4	WO ₃ nanoparticles ^b	0.52	190.5	49.9
5	WO ₃ nanobelts ^b	0.23	40.2	15.6
6	WO ₃ nanosheets ^b	0.09	136.5	9.8

^a The fresh catalysts. ^b The spent catalyst in the conversion of FA at 170 °C for 2 h.

nanoparticles have the highest specific surface area and biggest pore volume, followed by the WO₃ nanobelts and WO₃ nanosheets.

Fig. 1e shows the results of the PL analyses of the catalysts, by which the defects on the surface of WO_3 can be revealed. The PL peak at about 599 nm is due to oxygen vacancies and the peak intensity indicates the content of oxygen vacancies.^{24,25} This shows that all samples have a certain content of surface oxygen defects. Compared with WO_3 nanosheets, both WO_3 nanobelts and WO_3 nanoparticles had more oxygen defects, which might be beneficial to the production of acid sites. EPR can further prove the existence of oxygen defects and the different contents among the samples. It is believed that the signal at $g = 2.002$ can be attributed to an oxygen vacancy capturing an electron. As shown in Fig. S3 (ESI[†]), the evident peaks of the WO_3 nanobelts and WO_3 nanoparticles reveal the presence of a larger content of oxygen vacancies in comparison with the WO_3 nanosheets. It could be speculated that the WO_3 nanobelts and nanoparticles have a reduced number of W coordinated oxygen atoms on their respective exposed surfaces due to the presence of oxygen vacancies, which generally have positive charges. It is thus easy to form low valence W^{5+} , which might be beneficial to the formation of Lewis acid sites.²⁶ This will be discussed in the subsequent section of acid sites. Besides, the surface oxygen defects affected the distribution of the surface atoms, and also could influence the distribution of the acid sites and functionalities, which can be further revealed by FTIR.

The FTIR spectra shown in Fig. 1f indicate that the functional groups over the WO_3 catalysts display little difference in the range of $1000\text{--}4000\text{ cm}^{-1}$. However, the intensity of groups such as hydroxyl ($-\text{OH}$) on the surface of the WO_3 catalysts is varied. The presence of $-\text{OH}$ including terminal and bridging

$-\text{OH}$ can act as Brønsted acid sites.²⁷ Besides, the peak at 678 nm is assigned to the $\text{O}\text{--}\text{W}\text{--}\text{O}$ bond, which is the typical functional group of WO_3 .²⁸ The peak at 818 cm^{-1} can be attributed to the $\text{W}=\text{O}$ bond, and this could be related to the distribution of W and O atoms on the exposed facet of WO_3 .²⁸ To differentiate the distribution of W and O atoms on the different crystal planes, the peaks were fitted and the areas of the infrared absorption peaks are summarized in Fig. 1g and Table S1 (ESI[†]). The (001) faceted $\text{h}\text{--}\text{WO}_3$ has the highest content of $\text{O}\text{--}\text{W}\text{--}\text{O}$ bonds, followed by the (110) and (100) facets. Interestingly, the (001) facet has the lowest amount of $\text{W}=\text{O}$ bonds, and the (110) facet possesses the highest content of $\text{W}=\text{O}$ bonds, followed by the (100) facet. Compared with the $\text{O}\text{--}\text{W}$ bond, the vibration peak of the $\text{W}=\text{O}$ bond is located at a higher wavenumber, which shows a higher binding energy of $\text{W}=\text{O}$. The different contents of $\text{W}\text{--}\text{O}$ and $\text{W}=\text{O}$ on the different crystal planes indicate that the number of W atoms and O atoms can be different. For example, the total content of $\text{W}\text{--}\text{O}$ and $\text{W}=\text{O}$ bonds on the (100) facet of WO_3 is the lowest, which indicates that the (100) surface has low amount of surface acidic sites. Therefore, the content of $\text{W}\text{--}\text{O}$ and $\text{W}=\text{O}$ bonds on different surfaces can be an indication of the amount of surface acidic sites.

XPS measurements were used to characterize the chemical states and environments of W in the different WO_3 catalysts. As shown in Fig. S4 (ESI[†]), the survey spectrum shows that the peaks at 36.1 , 284.8 and 532.7 eV are assigned to $\text{W}4\text{f}$, $\text{C}1\text{s}$ and $\text{O}1\text{s}$, respectively.²⁹ The high resolution XPS spectra of $\text{W}4\text{f}$ for the different samples shown in Fig. 2a display an evident left

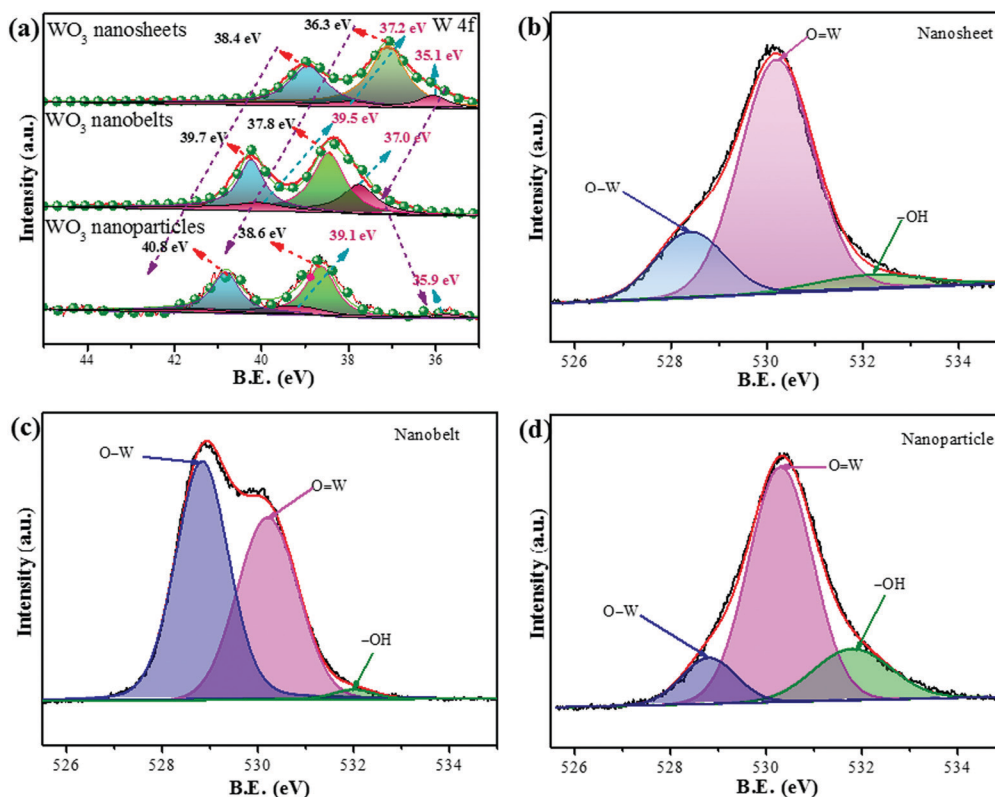


Fig. 2 XPS spectra of the $\text{h}\text{--}\text{WO}_3$ catalysts with different morphologies, (a) W 4f, and (b)–(d) O 1s.

shift, indicating the higher binding energy of W with O. In addition, the W4f peak can be divided into two sets of peaks, indicating different binding energies of W4f in the catalyst. The (001) faceted WO_3 nanosheets display two peaks at 38.4 eV($4f_{5/2}$) and 36.3 eV($4f_{7/2}$), which can be assigned to W^{6+} ;^{30,31} the peaks at 37.2 eV and 35.1 eV can be assigned to W^{5+} , which usually has a great correlation with oxygen vacancies.³² Compared with the (001) faceted WO_3 , the W^{6+} on the (100) facets shows two peaks at 39.7 eV and 37.8 eV, indicating that the W^{6+} on the (100) facets has higher binding energy. Especially, the (110) faceted WO_3 shows two peaks of W^{6+} at 40.8 eV and 38.6 eV, which is the highest binding energy of W^{6+} in the three facets. The higher content of W^{6+} reveals the higher content of strong Lewis acid sites, which might be beneficial to the reactivity of active sites on the surface of the catalyst.^{33,34}

As shown in Fig. 2b–d and Table S2 (ESI[†]), the change tendency of O1s is similar to that of W4f. The O1s XPS spectra of the WO_3 nanosheets can be deconvoluted into three peaks at 528.4, 530.2, and 532.2 eV, which can be attributed to O–W–O, W=O and –OH, respectively. In addition, the O1s binding energy shifts to higher binding energy and follows the sequence of nanosheets, nanobelts, and nanoparticles, indicating higher energy for the exposed facet. Importantly, the content of hydroxyl groups (see Table S2, ESI[†]) follows the sequence of nanosheets < nanobelts < nanoparticles, which indicates that the WO_3 sphere exposed (110) facet possesses the highest content of Brønsted acid sites.³⁵

Acid site analysis

The results of the distribution of the acidic sites with the NH_3 -TPD technique are shown in Fig. 3. The weak, moderate, and strong acidic sites are located in the range less than 200, 200–400, and above 400 °C, respectively. Both the WO_3 nanosheets and nanobelts exhibit a wide temperature region for NH_3 desorption, especially for the WO_3 nanosheets, indicating that there are various types of acid sites with distinct strengths on the surface of the catalyst.³⁶ However, the abundances of these acid sites are much lower than that in the WO_3 nanoparticles, as revealed from the Y-axis of Fig. 3a. Moreover, only two key peaks centered at

ca. 439 and 570 °C are observed in Fig. 3a. These results demonstrate that the acid strengths on the surface of the WO_3 nanoparticles are stronger and medium acidic sites, of which strong acidic sites predominate.^{37,38}

Fig. 3b shows the explicit distribution of acidic sites with different abundance for the three catalysts. Clearly, the acid sites are the most abundant in the WO_3 nanoparticles. More importantly, the strong acid sites are predominant on the surface of the WO_3 nanoparticles, while the weak and medium acid sites dominate on the surface of the WO_3 nanobelts or nanosheets, and the abundances are much lower than that in the WO_3 nanoparticles. It is worth noting that the WO_3 nanoparticles have the largest specific area, which might be responsible for the more abundant acid sites. Thus, the acid strengths were normalized by dividing by the specific area of the sample. The results in Fig. 3b indicate that the WO_3 nanoparticles have the highest abundance of acid sites. In combination with the analysis of XPS and the crystal structure (Fig. 4), it could be inferred that the O=W bonds with higher binding energy facilitate the formation of the acid sites on the (110) surface of WO_3 . Furthermore, the acid sites on the surface of WO_3 could possibly include both Lewis and Brønsted acid sites, which was further characterized with pyridine DRIFTS characterization.

Pyridine DRIFTS characterization of the samples was used to characterize the distribution of Lewis and Brønsted acid sites. As shown in Fig. S5c (ESI[†]), the spectrum of WO_3 nanoparticles contains several significant peaks at 1415, 1450, 1480, 1533 and 1598 cm^{-1} , which can be attributed to the chemisorption of molecular pyridine at different types of surface acidic sites.^{39–41} The peak at 1450 cm^{-1} can be ascribed to the pyridine adsorbed on Lewis acid sites, and the peak at 1533 cm^{-1} is due to the pyridine adsorbed on Brønsted acid sites. Besides, the peak at 1480 cm^{-1} is attributed to the pyridine adsorbed on Brønsted acidic sites and Lewis acidic sites.⁴²

The pyridine absorption peaks of the WO_3 nanosheets (Fig. S5b, ESI[†]) are similar to those of the WO_3 nanoparticles (Fig. S5c, ESI[†]) in terms of peak distribution. However, the peak intensities are much weaker, and the abundance of the acid

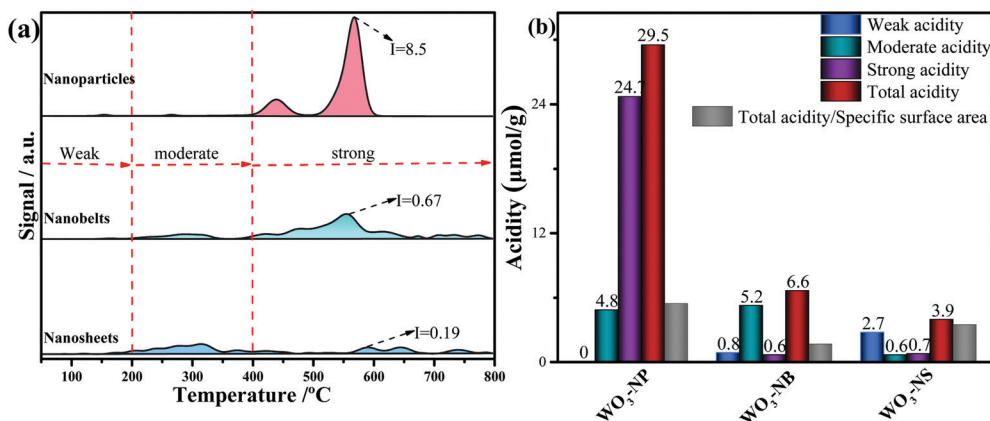


Fig. 3 (a) NH_3 -TPD spectra of the WO_3 catalysts with different morphologies, and (b) distribution of acidic sites over the WO_3 catalysts with different morphologies obtained by NH_3 -TPD (NH_3 uptake); WO_3 -NP: WO_3 nanoparticles; WO_3 -NB: WO_3 nanobelts; WO_3 -NS: WO_3 nanosheets.

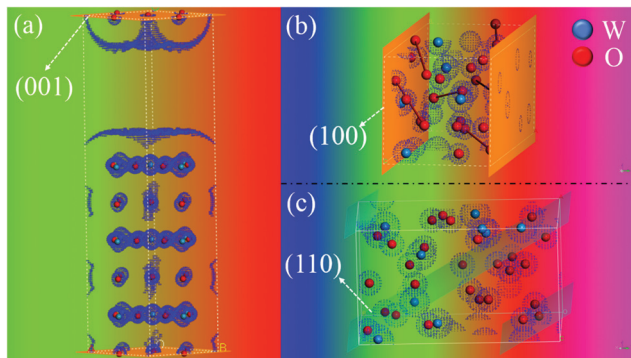


Fig. 4 Atomic structure arrangement of h-WO₃ with different crystal planes, (a) h-WO₃ nanosheets-(001)-P6/mmm 191, (b) h-WO₃ nanobelts-(100)-P63/mcm 193, and (c) h-WO₃ nanoparticles-(110)-P6/mmm 191. The model data was calculated according to the castep package of Materials Studio.

sites over the WO₃ nanosheets is remarkably lower, which is in line with the NH₃-TPD results. In contrast, the acid sites over the WO₃ nanoparticles could maintain high intensity after desorption, even when the temperature was elevated to 500 °C. This further confirms that the (110) faceted h-WO₃ nanoparticles have abundant strong acid sites.

The absorption peak belonging to the Brønsted acid sites is very weak compared with those of the Lewis acid sites, indicating that the (100) faceted WO₃ nanobelts mainly possess Lewis acid sites. In addition, the Brønsted acid sites over the (001) faceted WO₃ nanosheets are also much weaker than those of the (110) faceted h-WO₃ nanoparticles. The exposure of the (110) crystal plane of the catalyst, therefore, is closely related to the formation of strong Brønsted and Lewis acid sites on the surface of the catalyst. The exposure of the (100) and (001) facets promotes the formation of Lewis acid sites rather than strong Brønsted acid sites.

According to previous reports, the Lewis acid sites on the surface of WO₃ might be due to the presence of W⁵⁺/W⁶⁺ on the surface of WO₃.⁴³ Compared with the WO₃ nanosheets, it can be found that the binding energy of W⁶⁺ on both the (110) and (100) surfaces increased gradually (Fig. 2a), which leads to stronger binding between W⁶⁺ and O atoms on the surface. The higher binding energy of W⁶⁺ favors the formation of hydroxyl groups on the surface of the catalyst, thus boosting the formation of Brønsted acidic sites. Specifically, the binding energy of W⁶⁺ on the (110) surfaces, in comparison with the (100) and (001) surfaces, is higher, which causes the (110) facet of WO₃ to be more active and facilitates the presence of hydroxyl groups, forming strong Brønsted acid sites. Oxygen vacancies adsorb water molecules and thus can provide Brønsted acid sites on the (110) and (100) planes; therefore, more oxygen vacancies can provide more Brønsted acid sites on the facet of WO₃.

In addition, the density of states (DOS) on the different crystal planes also has an important influence on the distribution of acid sites (Fig. S6, ESI[†]). As shown in Fig. 4 and Fig. S6 (ESI[†]), the density functional theory (DFT) calculations of the

(100), (001) and (110) crystal facets showed that the (110) facet of WO₃ has a higher DOS, which indicates that the (110) facet is more reactive than the others are. These factors are favorable for the coexistence of Brønsted and Lewis acid sites. Brønsted and Lewis acid sites play highly distinct roles in acid-catalyzed reactions such as isomerization, dehydrations, *etc.*^{44–46} Brønsted acid sites including terminal and bridging hydroxyl groups can give protons, which promote the electrophilic reaction, while Lewis acid sites can adsorb reactant molecules. Thus, the synergetic effect of Brønsted and Lewis acid sites accelerates the reaction. The effects of the distinct distributions of the Brønsted and Lewis acid sites over the WO₃ catalysts, induced by the exposure of different facets, were further investigated in the catalytic conversion of FA to EL in ethanol.

Catalytic activity

Table 2 shows the distribution of the products from the conversion of FA at temperatures of 130, 150, 160, and 170 °C over the different WO₃ catalysts. At 130 °C, all the WO₃ catalysts show low activity due to the lower reaction temperature. With the increase of the reaction temperature to 170 °C, the conversion of FA and the yields of EL increase remarkably, especially over the WO₃ nanoparticles (Table 2, entry 6). The capability of the WO₃ catalysts for the catalytic conversion of FA to EL follows the order WO₃ nanoparticles > WO₃ nanobelts > WO₃ nanosheets. Although the conversion of FA reaches 100% over the WO₃ nanobelts, the yield of EL is only 37.3% (Table 2, entry 7). Most of the FA could be converted to polymers with the Lewis acid sites as the catalytic sites, which was further proved by UV-fluorescence spectra (Fig. S7b, ESI[†]).⁴⁷ Further increasing the reaction temperature, higher catalytic activities of the WO₃ catalysts can be obtained.

Table 2 Conversion of FA and yields of EL over the WO₃ catalysts with different morphologies^a

Entry	Tem. (°C)	Catalysts	Con. (FA, %)	Yield (EL, %)	Sel. (EL, %)
1	130	Blank	0.6	0	0
2		WO ₃ nanoparticles	34.7	8.1	23.4
3		WO ₃ nanobelts	18.8	6.4	34.1
4		WO ₃ nanosheets	0.4	0.0	0
5	150	Blank	2.1	0	0
6		WO ₃ nanoparticles	100	86.5	86.5
7		WO ₃ nanobelts	100	37.3	37.3
8		WO ₃ nanosheets	55.8	5.8	10.3
9	160	Blank	0.2	0.1	0
10		WO ₃ nanoparticles	100	88.0	88.0
11		WO ₃ nanobelts	92.6	67.8	73.3
12		WO ₃ nanosheets	92.7	35.8	38.7
13	170	Blank	3.1	0.3	9.7
14		WO ₃ nanoparticles	100	93.3	93.3
15		WO ₃ nanobelts	96.8	77.8	80.3
16		WO ₃ nanosheets	100	32.7	32.7

^a Reaction conditions: FA loaded: 0.4 mmol, absolute ethanol loaded: 3.96 g, catalyst loaded: 0.04 g, P₀(N₂) = 4 MPa (at room temperature), reaction time: 2 h.

The yield of EL reaches 93.3% over the WO_3 nanoparticles at 170 °C (Table 2, entry 14). The elevation of the reaction temperature also increases the catalytic activity of the WO_3 nanobelt catalyst as it contained some Brønsted acid sites that are reactive for the conversion of FA to EL.

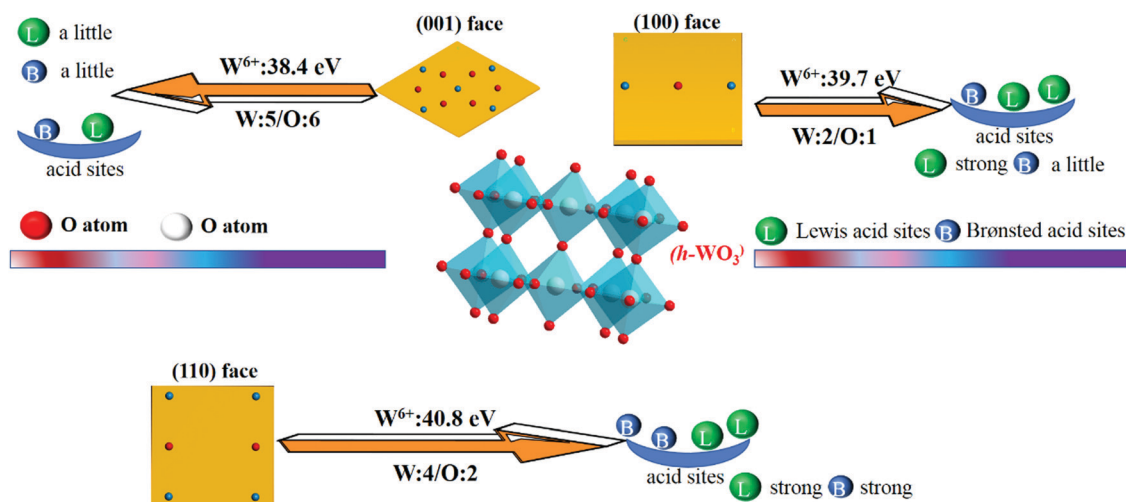
The high selectivity of EL over the WO_3 nanosheets could not be achieved at a reaction temperature of 160 and 170 °C, because the Lewis acidic sites over this catalyst mainly catalyzed the polymerization of FA. As shown in Fig. S7c (ESI[†]), the UV fluorescence characterizations show that the WO_3 nanosheets mainly catalyze the formation of polymers with π -conjugated structures with one to three polycyclic rings and a few π -conjugated polymers with three to five rings.⁴⁵ Compared with the WO_3 nanosheets and nanobelts, the WO_3 nanoparticles only catalyze FA to form a trace amount of polymer, which can be identified by the high yield of EL.

According to the abovementioned results, a schematic diagram of the relationship between the WO_3 catalyst structure and acid site distribution is proposed in Scheme 1, and the possible conversion paths from FA to EL under the catalysis of acid sites were put forward. The number and proportion of W atoms and oxygen atoms on the different exposed facets are different, which is determined by the different arrangement of atoms on the different crystal planes. As shown in Scheme 1, the (001) facet has the maximum number of atoms, which has been confirmed by the DOS, but oxygen atoms had a higher ratio, which may not be conducive to the exposure of surface W atoms. In addition, XPS data showed that W^{6+} on the (001) facet has a lower binding energy, which is disadvantageous to the adsorption of water to form hydroxyl groups. In other words, it is adverse to the presence of acidic sites on the surface. On the other hand, the W^{6+} on the (001) facet of WO_3 had strong Lewis acid sites, and the binding energy determines the acid strength to a certain extent. In contrast, although there are fewer atoms on the (100) facet in comparison with (001), the proportion of W atoms is higher than that on the (001) facet, which is also favorable for the presence of acidic sites on the surface.

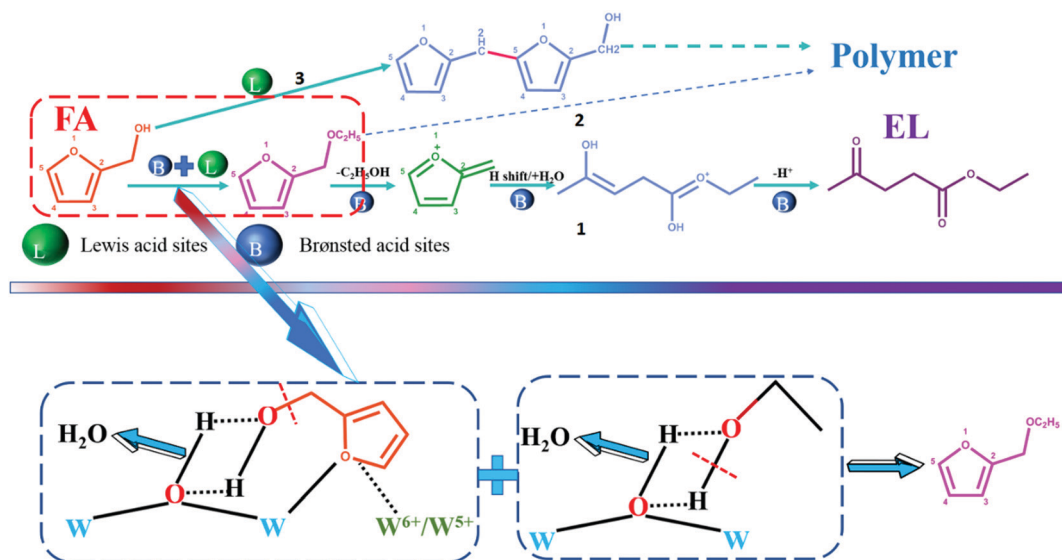
Interestingly, the (110) facet has a large number of atoms while maintaining a high proportion of W atoms, which is conducive to the exposure of tungsten atoms while maintaining high electron density. XPS data show that the binding energy of W^{6+} on the (110) facet is the highest, which is advantageous to the adsorption of water to form Brønsted acid sites on the surface. Therefore, the WO_3 (110) facet has very strong Brønsted and Lewis acid sites, and the (001) facet has only weak Lewis acid sites and Brønsted acid sites. In addition, oxygen defects and W^{5+} can act as weak Lewis acid sites compared with W^{6+} . Therefore, although there are certain amounts of oxygen vacancies and W^{5+} on the (001) facet, it still shows weak Lewis acidity. In other words, the contribution of oxygen vacancies and W^{5+} to the acidity on the WO_3 surface was small.

Reaction mechanism

To further explore the reaction mechanism on a molecular level, *in situ* infrared simulations of the conversion of furfuryl alcohol were carried out. As shown in Fig. 6a, the FT-IR spectra of ethyl levulinate (EL) showed the unique C=O bond vibration, which could be used as a symbol for the formation of ethyl levulinate. Then, as shown in Fig. 6b, the peak at 3346 cm^{-1} was assigned to the -OH bond, which was linked to ethyl alcohol. With the reaction time reaching 20 min, the hydroxyl peak representing alcohol significantly decreased, while the peak representing EL began to increase. Besides, the peak at 3612 cm^{-1} was assigned to the -OH bond of the intermediate in the conversion of furfuryl alcohol to EL. Therefore, the possible conversion path of FA to LA is shown in Scheme 2. FA could convert to EL under the synergetic effect of Lewis and Brønsted acid sites. Lewis acid sites facilitate the adsorption of reactant molecules on the catalyst surface, while Brønsted acid sites provide protons, promoting the conversion from FA to EL. However, if there are few Brønsted acid sites on the surface of the catalyst or in the presence of weak Brønsted acid sites, it would be converted to the polymer through reaction route 2 or 3 under the catalysis of Lewis acid sites. Therefore, the (100)



Scheme 1 Relationship between the WO_3 catalyst structure and acid site distribution.



Scheme 2 The conversion of furfuryl alcohol to ethyl levulinate under the action of acid sites.

face of WO_3 with strong Lewis acid sites is more prone to catalyze the conversion of FA to polymers. The (110) facet with

strong Lewis acid sites and Brønsted acid sites could promote the efficient conversion of FA to EL.

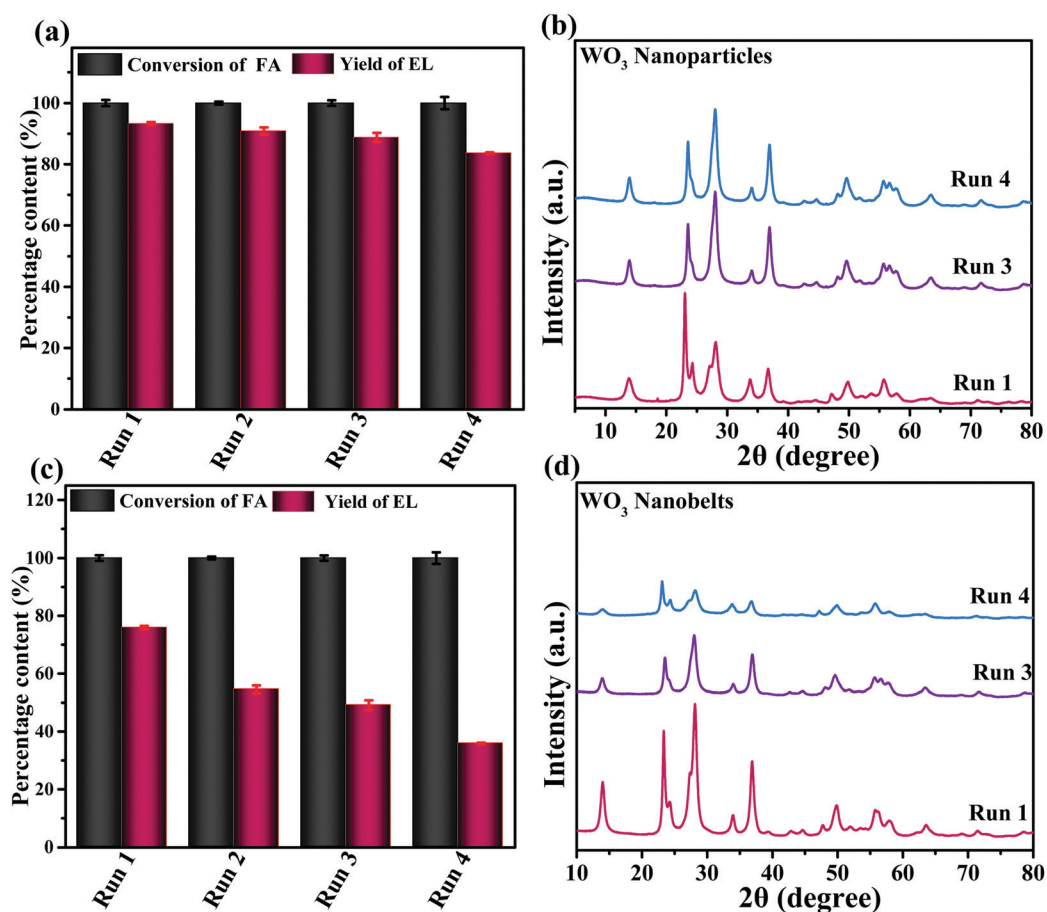


Fig. 5 Recyclability tests of the conversion of FA to EL catalyzed by WO_3 catalysts with different morphologies. (a) Conversion of FA and yield of EL catalyzed by WO_3 nanoparticles, (b) XRD patterns of the WO_3 nanoparticle catalyst after four runs at 170 °C, (c) conversion of FA catalyzed by WO_3 nanobelts, and (d) XRD patterns of the WO_3 nanobelt catalyst after four cycles at 170 °C. (Reaction conditions: FA loaded: 0.4 mmol, ethanol loaded: 3.6 g, catalyst loaded: 0.04 g, $P_{\text{O}_2}(\text{N}_2) = 4$ MPa (at room temperature), $T = 170$ °C, reaction time: 2 h).

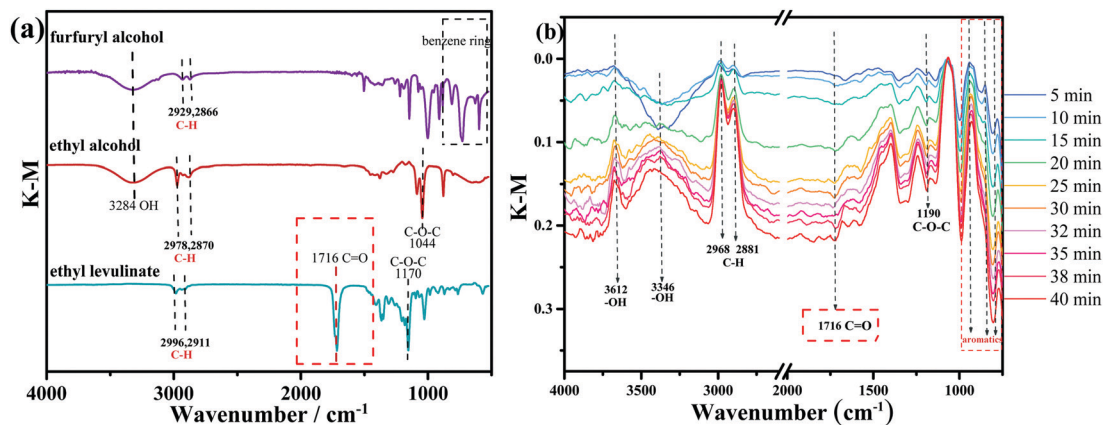


Fig. 6 (a) FT-IR spectra of furfuryl alcohol, ethyl alcohol, and ethyl levulinate. (b) FT-IR changes in the conversion of furfuryl alcohol to ethyl levulinate at 150 °C in N₂.

Catalytic reusability

The recyclability of the catalyst is shown in Fig. 5. The (110) faceted WO₃ nanoparticles exhibit excellent catalytic activity after four runs. The conversion of FA is maintained at 100% while the yield of EL changes slightly. The XRD results for the used catalysts in Fig. 5b show that the WO₃ nanoparticles could maintain a classical h-structure and higher crystallinity after four cycles, indicating the stable structure of the catalysts.⁴⁸ Furthermore, the TEM results demonstrate that the WO₃ nanoparticles display an unchanged spherical morphology (Fig. S1, ESI[†]) after four cycles compared with the pristine catalyst. This further confirms the stable microstructure and morphology of the WO₃ nanoparticles. Besides, the results of FTIR are also consistent with the XRD and TEM characterization (Fig. S8, ESI[†]). In comparison, the WO₃ nanobelts cannot maintain stable catalytic performances. Although the conversion of FA is 100%, the catalyst deactivated progressively with one cycle of reuse. The XRD results show reduced crystallinity of the WO₃ nanobelts, due to the highly weakened diffraction peaks (Fig. 5). The TEM results indicate the substantial change of the morphology (Fig. S1, ESI[†]). The BET measurements of the WO₃ nanobelts also show the drastic decrease of the specific area (Table 1, entry 6). These results together indicate that the WO₃ nanobelts with the (100) facet exposed were not stable in ethanol. The exposure of the (100) facets induces the formation of the Lewis acid sites as the predominant acid sites and the instability of the catalyst. In comparison, the exposure of the (110) facet in the WO₃ nanoparticles results in the formation of the desirable Brønsted acidic sites and the superior stability under subcritical conditions, which was more suitable for effective acid-catalyzed conversion of FA to EL. The W⁶⁺ on the (110) facet of WO₃ has high binding energy, which could make the W–O bonding more stable, which may be beneficial to improve the stability of acid sites.⁴⁹

Conclusions

In summary, WO₃ nanoparticles, nanobelts, and nanosheets with different exposed facets were prepared. The exposure of

varied facets influenced the distribution of acid sites and the catalytic activity in conversion of FA to EL. The WO₃ nanoparticles had not only the highest specific surface area but also the highest abundance of acidic sites. The XPS and DFT calculation results indicated that the nanoparticles with the (110) facet exposed had a high DOS and more W atoms with the highest binding energy on the surface, which was conducive to the preservation of acidic hydroxyl groups, rendering the formation of Brønsted acidic sites with high strength. The lower binding energy of W⁶⁺ over the (001) faceted WO₃ nanosheets and (100) faceted WO₃ nanobelts, in comparison with (110) faceted WO₃, does not favor the generation of strong Lewis acid sites. The Lewis acidic sites over the WO₃ nanosheet and nanobelt catalysts could not effectively catalyze the conversion of FA to EL, but catalyzed the polymerization of FA. The strong Brønsted acidic sites over the WO₃ nanoparticles catalyzed the selective conversion of FA to EL with the yield reaching 93.3% under the optimum conditions. Moreover, the WO₃ nanoparticles showed high catalytic performances in the recyclability tests, while the WO₃ nanobelts could not maintain the crystallinity and the morphology, and deactivated quickly. The results herein demonstrated the correlations of the exposed facets with the type and abundance of the acidic sites formed. In addition to WO₃, the exposure of varied facets in other oxides could also impact the distribution of the acidic sites and deserves intensive attention.

Abbreviations

EL	Ethyl levulinate
FA	Furfuryl alcohol
XRD	X-ray diffraction
TEM	Transmission electron microscopy
HRTEM	High resolution transmission electron microscopy
PL	Photoluminescence
EPR	Electron paramagnetic resonance
BET	Brunauer–Emmett–Teller

FTIR	Fourier transform infrared
DRIFTS	Diffuse reflectance infrared Fourier transform spectroscopy
NH ₃ -TPD	Temperature programmed desorption with ammonia
GC-MS	Gas chromatography coupled with mass spectrometry
XPS	X-ray photoelectron spectroscopy

Conflicts of interest

There are no conflicts to declare.

Acknowledgements

This work was supported by National Natural Science Foundation of China (No. 51876080), the Program for Taishan Scholars of Shandong Province Government, the Agricultural Innovation Program of Shandong Province (SD2019NJ015) and the R & D program of Shandong Basan Graphite New Material Plant. Besides, National Natural Science Foundation of China (21477047) could also provide help for this work.

References

- P. A. Shinde, A. C. Lokhande, N. R. Chodankar, A. M. Patil, J. H. Kim and C. D. Lokhande, Temperature dependent surface morphological modifications of hexagonal WO₃ thin films for high performance supercapacitor application, *Electrochim. Acta*, 2017, **224**, 397–404.
- L. Cui, X. Ding, Y. Wang, H. Shi, L. Huang, Y. Zuo and S. Kang, Facile preparation of Z-scheme WO₃/g-C₃N₄ composite photocatalyst with enhanced photocatalytic performance under visible light, *Appl. Surf. Sci.*, 2017, **391**, 202–210.
- J. Jin, J. Yu, D. Guo, C. Cui and W. Ho, A hierarchical Z-scheme CdS-WO₃ photocatalyst with enhanced CO₂ reduction activity, *Small*, 2015, **11**(39), 5262–5271.
- W.-T. Koo, S.-J. Choi, N.-H. Kim, J.-S. Jang and I.-D. Kim, Ultra-Sensitive H₂S Gas Sensor Based on WO₃ Nanocubes with Low Operating Temperature, *Sens. Actuators, B*, 2016, **223**, 301–310.
- M. Martins, J. Milikić, B. Šljukić, G. S. Soylu, A. B. Yurtecan, G. Bozkurt and D. M. Santos, Mn₂O₃-MO (MO = ZrO₂, V₂O₅, WO₃) supported PtNi nanoparticles: Designing stable and efficient electrocatalysts for oxygen reduction and borohydride oxidation, *Microporous Mesoporous Mater.*, 2019, **273**, 286–293.
- R. Zhao, X. Li, J. Su and X. Gao, Preparation of WO₃/g-C₃N₄ composites and their application in oxidative desulfurization, *Appl. Surf. Sci.*, 2017, **392**, 810–816.
- Y. M. Hunge, M. A. Mahadik, A. V. Moholkar and C. H. Bhosale, Photoelectrocatalytic degradation of oxalic acid using WO₃ and stratified WO₃/TiO₂ photocatalysts under sunlight illumination, *Ultrason. Sonochem.*, 2017, **35**, 233–242.
- S. G. Kumar and K. K. Rao, Comparison of modification strategies towards enhanced charge carrier separation and photocatalytic degradation activity of metal oxide semiconductors (TiO₂, WO₃ and ZnO), *Appl. Surf. Sci.*, 2017, **391**, 124–148.
- I. Jiménez-Morales, J. Santamaría-González, P. Maireles-Torres and A. Jiménez-López, Zirconium doped MCM-41 supported WO₃ solid acid catalysts for the esterification of oleic acid with methanol, *Appl. Catal., A*, 2010, **379**(1–2), 61–68.
- W. Xie and T. Wang, Biodiesel production from soybean oil transesterification using tin oxide-supported WO₃ catalysts, *Fuel Process. Technol.*, 2013, **109**, 150–155.
- A. Ulgen and W. F. Hoelderich, Conversion of glycerol to acrolein in the presence of WO₃/TiO₂ catalysts, *Appl. Catal., A*, 2011, **400**(1–2), 34–38.
- B. Ren, M. Fan, J. Wang and X. Jing, Preparation and application of magnetic solid acid SO₄²⁻/ZrO₂/Fe₃O₄/WO₃ for synthesis of fructose, *Solid State Sci.*, 2011, **13**(8), 1594–1598.
- A. A. Costa, P. R. Braga, J. L. De Macedo, J. A. Dias and S. C. Dias, Structural effects of WO₃ incorporation on USY zeolite and application to free fatty acids esterification, *Microporous Mesoporous Mater.*, 2012, **147**(1), 142–148.
- C. Zhang, T. Liu, H. J. Wang, F. Wang and X. Y. Pan, Synthesis of acetyl salicylic acid over WO₃/ZrO₂ solid superacid catalyst, *Chem. Eng. J.*, 2011, **174**(1), 236–241.
- S. Wang, H. Chen, G. Gao, T. Butburee, M. Lyu, S. Thaweesak, J. Yun, A. Du, G. Liu and L. Wang, Synergistic crystal facet engineering and structural control of WO₃ films exhibiting unprecedented photoelectrochemical performance, *Nano Energy*, 2016, **24**, 94–102.
- Y. Yao, F. Ji, M. Yin, X. Ren, Q. Ma, J. Yan, S. Zhong and F. Liu, Ag Nanoparticle-Sensitized WO₃ Hollow Nanosphere for Localized Surface Plasmon Enhanced Gas Sensors, *ACS Appl. Mater. Interfaces*, 2016, **8**(28), 18165–18172.
- X. Wang, H. Fan and P. Ren, Effects of exposed facets on photocatalytic properties of WO₃, *Adv. Powder Technol.*, 2017, **28**(10), 2549–2555.
- Y. Wang, J. Yang, R. Gu, L. Peng, X. Guo, N. Xue, Y. Zhu and W. Ding, Crystal-Facet Effect of γ -Al₂O₃ on Supporting CrO_x for Catalytic Semihydrogenation of Acetylene, *ACS Catal.*, 2018, **8**(7), 6419–6425.
- Y. Zheng, G. Chen, Y. Yu, Y. Hu, Y. Feng and J. Sun, Urea-assisted synthesis of ultra-thin hexagonal tungsten trioxide photocatalyst sheets, *J. Mater. Sci.*, 2015, **50**(24), 8111–8119.
- J. Wang, Z. Chen, G. Zhai and Y. Men, Boosting photocatalytic activity of WO₃ nanorods with tailored surface oxygen vacancies for selective alcohol oxidations, *Appl. Surf. Sci.*, 2018, **462**, 760–771.
- X. T. Su, F. Xiao, J. L. Lin, J. K. Jian, Y. N. Li, Q. J. Sun and J. D. Wang, Hydrothermal synthesis of uniform WO₃ sub-microspheres using thiourea as an assistant agent, *Mater. Charact.*, 2010, **61**(8), 831–834.
- P. A. Shinde, A. C. Lokhande, N. R. Chodankar, A. M. Patil, J. H. Kim and C. D. Lokhande, Temperature dependent

- surface morphological modifications of hexagonal WO₃ thin films for high performance supercapacitor application, *Electrochim. Acta*, 2017, **224**, 397–404.
- 23 L. Czepirski, M. R. Balys and E. Komorowska-Czepirska, Some generalization of Langmuir adsorption isotherm, *Int. J. Chem.*, 2000, **3**(14), 1099–8292.
 - 24 Y. Bu, Z. Chen and C. Sun, Highly efficient Z-Scheme Ag₃PO₄/Ag/WO_{3-x} photocatalyst for its enhanced photocatalytic performance, *Appl. Catal., B*, 2015, **179**, 363–371.
 - 25 R. Zhang, F. Ning, S. Xu, L. Zhou, M. Shao and M. Wei, Oxygen vacancy engineering of WO₃ toward largely enhanced photoelectrochemical water splitting, *Electrochim. Acta*, 2018, **274**, 217–223.
 - 26 J. Chai, S. Zhu, Y. Cen, J. Guo, J. Wang and W. Fan, Effect of tungsten surface density of WO₃-ZrO₂ on its catalytic performance in hydrogenolysis of cellulose to ethylene glycol, *RSC Adv.*, 2017, **7**(14), 8567–8574.
 - 27 X.-Z. Guo, Y.-F. Kang, T.-L. Yang and S.-R. Wang, Low-temperature NO₂ sensors based on polythiophene/WO₃ organic-inorganic hybrids, *Trans. Nonferrous Met. Soc. China*, 2012, **22**(2), 380–385.
 - 28 Z. Wang, S. Zhou and L. Wu, Preparation of rectangular WO₃-H₂O nanotubes under mild conditions, *Adv. Funct. Mater.*, 2007, **17**(11), 1790–1794.
 - 29 A. P. Shpak, A. M. Korduban, M. M. Medvedskij and V. O. Kandyba, XPS studies of active elements surface of gas sensors based on WO_{3-x} nanoparticles, *J. Electron Spectrosc. Relat. Phenom.*, 2007, **156**, 172–175.
 - 30 Y. Li, Z. Liu, M. Ruan, Z. Guo and X. Li, 1D WO₃ nanorods/2D WO_{3-x} nanoflakes homojunction structure for enhanced charge separation and transfer towards efficient photoelectrochemical performance, *ChemSusChem*, 2019, **12**(24), 5282–5290.
 - 31 Z. Wang, D. Chu, L. Wang, L. Wang, W. Hu, X. Chen, H. Yang and J. Sun, Facile synthesis of hierarchical double-shell WO₃ microspheres with enhanced photocatalytic activity, *Appl. Surf. Sci.*, 2017, **396**, 492–496.
 - 32 S. Kim, S. Park, S. Park and C. Lee, Acetone sensing of Au and Pd-decorated WO₃ nanorod sensors, *Sens. Actuators, B*, 2015, **209**, 180–185.
 - 33 K. E. Ahmed, D. H. Kuo, M. A. Zeleke, O. A. Zelekew and A. K. Abay, Synthesis of Sn-WO₃/g-C₃N₄ composites with surface activated oxygen for visible light degradation of dyes, *J. Photochem. Photobiol., A*, 2019, **369**, 133–141.
 - 34 Z. Yang, C. Zhu, Z. Hou and P. Peng, Effect of oxygen vacancies on the surface morphology and structural properties of WO_{3-x} nanoparticles, *Mater. Express*, 2019, **9**(7), 773–777.
 - 35 A. V. Salkar, R. X. Fernandes, S. V. Bhosale and P. P. Morajkar, NH- and CH-Substituted Ureas as Self-Assembly Directing Motifs for Facile Synthesis and Electrocapacitive Applications of Advanced WO_{3-x} One-Dimensional Nanorods, *ACS Appl. Energy Mater.*, 2019, **2**(12), 8724–8736.
 - 36 C. Li, Z. Huang, Y. Chen, X. Liu, J. Chen, W. Qu, Z. Ma and X. Tang, Optimizing Selective Catalytic Reduction of NO with NH₃ on Fe₂O₃/WO₃ via Redox-Acid Synergy, *ChemCatChem*, 2018, **10**(18), 3990–3994.
 - 37 Y. Aponte and H. de. Lasa, The effect of Zn on offretite zeolite properties: Acidic characterizations and NH₃-TPD desorption models, *Ind. Eng. Chem. Res.*, 2017, **56**(8), 1948–1960.
 - 38 Y. Shao, K. Sun, Q. Li, Q. Liu, S. Zhang, Q. Liu, G. Hu and X. Hu, Copper-based catalysts with tunable acidic and basic sites for the selective conversion of levulinic acid/ester to γ -valerolactone or 1, 4-pentanediol, *Green Chem.*, 2019, **21**, 4499–4511.
 - 39 S. Triwahyono, T. Yamada and H. Hattori, IR study of acid sites on WO₃-ZrO₂ and Pt/WO₃-ZrO₂, *Appl. Catal., A*, 2003, **242**(1), 101–109, DOI: 10.1016/S0926-860X(02)00523-9.
 - 40 H. Sheng, H. Zhang, W. Song, H. Ji, W. Ma, C. Chen and J. Zhao, Activation of water in titanium dioxide photocatalysis by formation of surface hydrogen bonds: an in situ IR spectroscopy study, *Angew. Chem., Int. Ed.*, 2015, **54**(20), 5905–5909, DOI: 10.1002/ange.201412035.
 - 41 H. Hattori and Y. Ono, *Solid acid catalysis*, Shanghai, Fudan University Press, 2015.
 - 42 Q. Wang, G. Wang, H. Xin, J. Liu, G. Xiong, P. Wu and X. Li, Sn-doped Pt catalyst supported on hierarchical porous ZSM-5 for the liquid-phase hydrogenation of cinnamaldehyde, *Catal. Sci. Technol.*, 2019, **9**(12), 3226–3237.
 - 43 T. M. Peruzzolo, J. F. Stival, L. M. Baika, L. P. Ramos, M. T. Grassi, M. L. Rocco and M. S. Nakagaki, Efficient esterification reaction of palmitic acid catalyzed by WO_{3-x}/mesoporous silica, *Biofuels*, 2020, 1–11.
 - 44 D. D. Anggoro and N. A. S. Amin, Methane to liquid hydrocarbons over tungsten-ZSM-5 and tungsten loaded Cu/ZSM-5 catalysts, *J. Nat. Gas Chem.*, 2006, **15**(4), 340–347.
 - 45 R. Weingarten, G. A. Tompsett, Jr., C. W. Conner and G. W. Huber, Design of solid acid catalysts for aqueous-phase dehydration of carbohydrates: The role of Lewis and Brønsted acid sites, *J. Catal.*, 2011, **279**(1), 174–182.
 - 46 A. Takasu, Y. Narukawa and T. Hirabayashi, Polymerization of Nonfood Biomass-Derived Monomers to Sustainable Polymers, *J. Polym. Sci., Part A: Polym. Chem.*, 2006, **44**(18), 5247–5253.
 - 47 K. Sun, L. Zhang, Q. Xu, Z. Zhang, Y. Shao, D. Dong, G. Gao, Q. Liu, S. Wang and X. Hu, Evidence for cross-polymerization between the biomass-derived furans and phenolics, *Renewable Energy*, 2020, **154**, 517–531.
 - 48 B. Yu, J. N. Xie, C. L. Zhong, W. Li and L. N. He, Copper (I)@carbon-catalyzed carboxylation of terminal alkynes with CO₂ at atmospheric pressure, *ACS Catal.*, 2015, **5**(7), 3940–3944.
 - 49 P. Chen, M. Baldwin and P. R. Bandaru, Hierarchically structured, oxygen deficient, tungsten oxide morphologies for enhanced photoelectrochemical charge transfer and stability, *J. Mater. Chem. A*, 2017, **5**(28), 14898–14905.